River Flow 2010 - Dittrich, Koll, Aberle & Geisenhainer (eds) - © 2010 Bundesanstalt für Wasserbau ISBN 978-3-939230-00-7

Effect of Abutment Length on the Bed Shear Stress and the Horseshoe Vortex System

M. Koken & M. Gogus
Civil Engineering Department, Middle East Technical University, Ankara, Turkey

ABSTRACT: Turbulent flow structures forming around isolated bridge abutments with curved toes are investigated in this study. Detached Eddy Simulation (DES) at a channel Reynolds number of 45,000 is used. Channel bottom is taken to be horizontal which corresponds to the initiation of the scouring process. Incoming flow in the simulations were fully turbulent containing unsteady velocity fluctuations. Changes in the structure of the horseshoe vortex system and the bed shear stress and pressure r.m.s. fluctuations on the bed is investigated for two different abutment lengths. These quantities are very important in sediment entrainment and can be used to identify the possible erosion regions on the bed. Although the pattern of the bed shear stress is similar in both cases there are some quantitative differences. This is mainly because of the changes in the strength of the main necklace vortex forming around the abutment and due to the different blockage ratio at the cross-section where the abutment is attached. At both lengths the mean pressure r.m.s. fluctuations on the bed peaked beneath the separated shear layers.

Keywords: Bridge abutment, Turbulence, DES, Horseshoe vortex system, Bed shear stress.

1 INTRODUCTION

Bridge abutments cause development of a very complex three dimensional flow field within their proximity. This is mainly as a result of the separation of the incoming boundary layer. As flow approaches the abutment, because of the adverse pressure gradient, the boundary layer separates and the necklace shaped vortical structures (so called horseshoe vortex (HV) system) develop close to the bed which wraps around the abutment. In case the abutment lies on top of an erodible bed HV system play an important role in the formation of the local scour around this structure.

Although there are various experimental studies concentrated on the prediction of the scouring pattern and the maximum scour forming around different abutment geometries (see Melville 1997 for a review) not much work is done to identify the flow physics related to the scouring mechanism. Eddy resolving numerical simulations such as LES (Large Eddy Simulation) or DES provide 3D detailed solution of the flow field not only for the instantaneous but also for the mean flow field including turbulent statistics.

Koken and Constantinescu (2008a, 2008b) provided the first in-depth study of the structure and the unsteady dynamics of the flow field forming around vertical wall abutments both for flat bed and deformed bed conditions. They used a well resolved LES to simulate the flow field around the vertical wall abutment at a Reynolds number of 18,000 for both flat bed and deformed bed conditions (Koken and Constantinescu 2008a, 2008b).

The turbulent HV system around abutments is very unsteady and subject to large temporal variations of its location, size and intensity. Furthermore, the turbulent kinetic energy (TKE) and pressure r.m.s. fluctuations are significantly amplified within the HV system and large bed shear stress and pressure fluctuations are induced on the bed region beneath the HV system. (e.g., see Koken and Constantinescu, 2008a).

The present study focuses on the changes within the HV system and the bed shear stress around isolated abutments with different lengths. Abutments used in the present study have vertical lateral walls with a semi-cylindrical toe.

2 EXPERIMENTAL SETUP

Experiments were conducted in a 25 m long flume that has a width of 1.5 m and a height of 0.5 m. Sediment which has a median particle size, d_{50} = 1.5 mm, were stick on the channel bed for roughness. In each experiment, an abutment with different length (15 cm and 35 cm) which has a width of 10 cm was connected vertically to the side wall of the flume. The toe of the abutment was semi-cylindrical having a diameter of 10 cm. The channel Reynolds number which is defined by the approach velocity (U = 0.335 m/s) and the channel depth (D = 0.135 m) was approximately Re = 45,000. The abutment which has a length of 15 cm will be called as the short-abutment and the one which has a length of 35 cm will be called as the long abutment throughout the text.

Velocity measurements were taken at various points around the abutment at the mid flow depth using Micro-ADV (Acoustic Doppler Velocimetry) for validating the numerical results.

3 NUMERICAL MODEL

Eddy resolving models such as LES and DES are much more successful in the prediction of the massively separated flows compared with the conventional RANS models. In the present study, DES without wall functions is used to simulate the flow. A general description of the code used in this study is given by Constantinescu and Squires (2004).

The length scale is selected to be the flow depth (D) whereas the mean approach velocity (U) is used as the velocity scale. The length and width of the domain is selected to be 48D and 11.11D respectively. Abutment lengths, including the curved toe, were 1.11D and 2.59D for the two cases simulated and they are located at a 8D distance from the inlet section. The computational domain contained approximately 4 million nodes with a minimum grid spacing of $\Delta y^+ = y u_\tau/\nu \sim 1$ wall units (assuming that $u_\tau/U = 0.04$) in the normal direction to all the solid boundaries (See Figure-1).

Turbulent inflow conditions containing velocity fluctuations are obtained from a LES simulation held in a periodic channel and stored in a file. This is then fed into the inflow section of the DES simulation which contains the abutment in a time-accurate fashion. Free surface is modeled as a rigid lid whereas no slip boundary condition is used on all the solid surfaces. At the outflow a convective boundary condition is used which allowed the exit of the coherent structures from the domain in a time accurate way without producing unphysical oscillations. Non-dimensional time step used in the simulations were 0.025 D/U. The simulations were run on 12 processors in a PC Cluster.

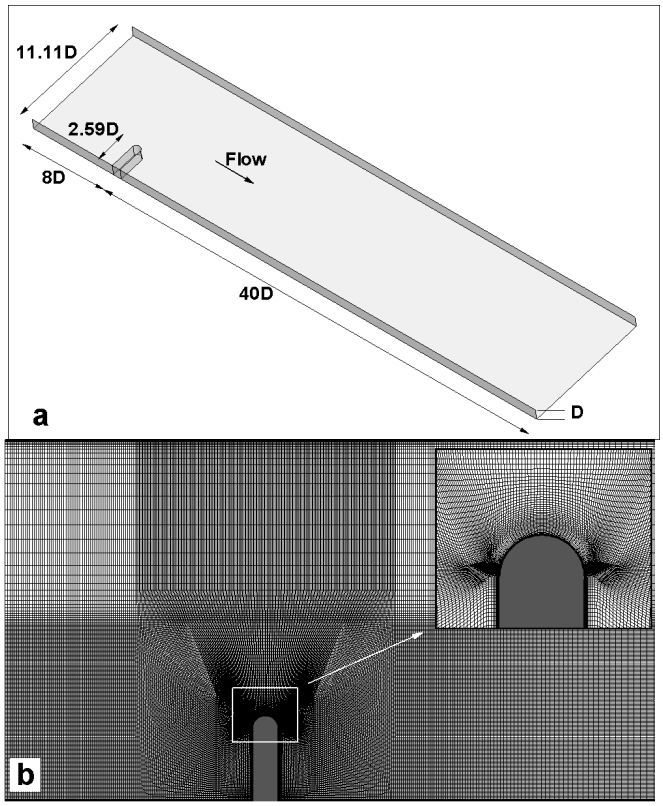

Figure 1. a) Computational domain b) Structured grid for Long-abutment.

4 RESULTS

4.1 *Validation*

Velocity timeseries were recorded at the mid flow depth for a duration of 30 seconds at various points (located approximately 2-5 cm apart from each other) around the abutment using Micro-ADV (Acoustic Doppler Velocimetry). The average velocity field is then obtained using these data sets.

Average streamwise velocity components obtained from the experiment and the simulation at the mid-depth are compared for case L-A in Figure-2. Note that there is a blank region close to the sidewall on which the abutment is attached on Figure-2b. This is the region on which velocity measurements were not taken because of the limitations of the ADV probes. In general, the experimental results show good agreement with the numerical results. Velocity magnitudes and the patterns are very similar.

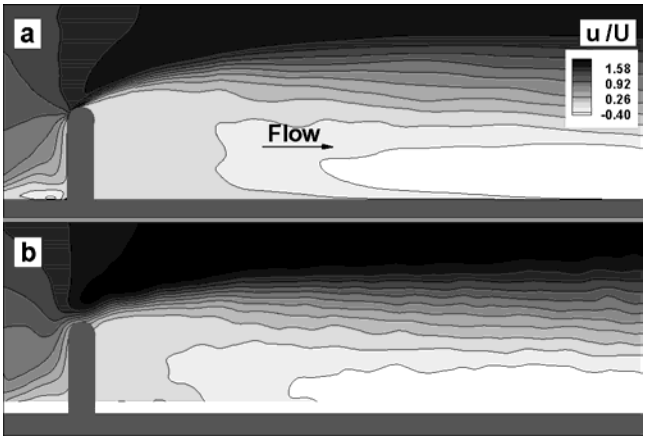

Figure 2. Average streamwise velocity at mid-depth obtained from: a) Numerical simulation; b) Experiment.

4.2 *Horseshoe Vortex System*

Coherent structures at the upstream of the abutment together with the HV system is visualized using Q criterion for the mean flow for short and long abutments in Figure-3 (note that the separated shear layers are covered in this figure). Mean horseshoe vortex system consists of three necklace vortices wrapping around the short and long abutments. In both cases, the primary horseshoe vortex, HV1, originates close to the side wall-abutment junction line and then follows the upstream face of the abutment. Getting closer to the abutment tip it bends towards the flow direction. On the other hand, the secondary and tertiary horseshoe vortices HV2 and HV3 originate at a further distance from the upstream abutment face, behind the recirculating flow. Getting closer to the tip of the abutment they also bend in the flow direction but this bending is much smoother compared to HV1.

Similar to the findings of Koken and Constantinescu (2008a), in both cases there is a coherent corner vortex, CV, at the upstream recirculation region which originates from the free surface and goes into the deeper flow depths where it bends and eventually merges with the primary necklace vortex HV1. Corner vortex CV, convects additional fluid and momentum from the regions close to the free surface into the core of the primary necklace vortex HV1.

Comparing the short and long abutment cases, there are important differences in the organization and the coherence of the HV system described above. Compared to the long abutment case in the short abutment case the primary necklace vortex HV1 is coherent at a relatively smaller length. This vortex completely diffuses within the flow at a distance approximately 1D downstream of the abutment. On the other hand, in the long abutment case this vortex is much stronger and it remains coherent at a much longer length until it completely diffuses within the flow (at approximately 17D downstream of the abutment axis).

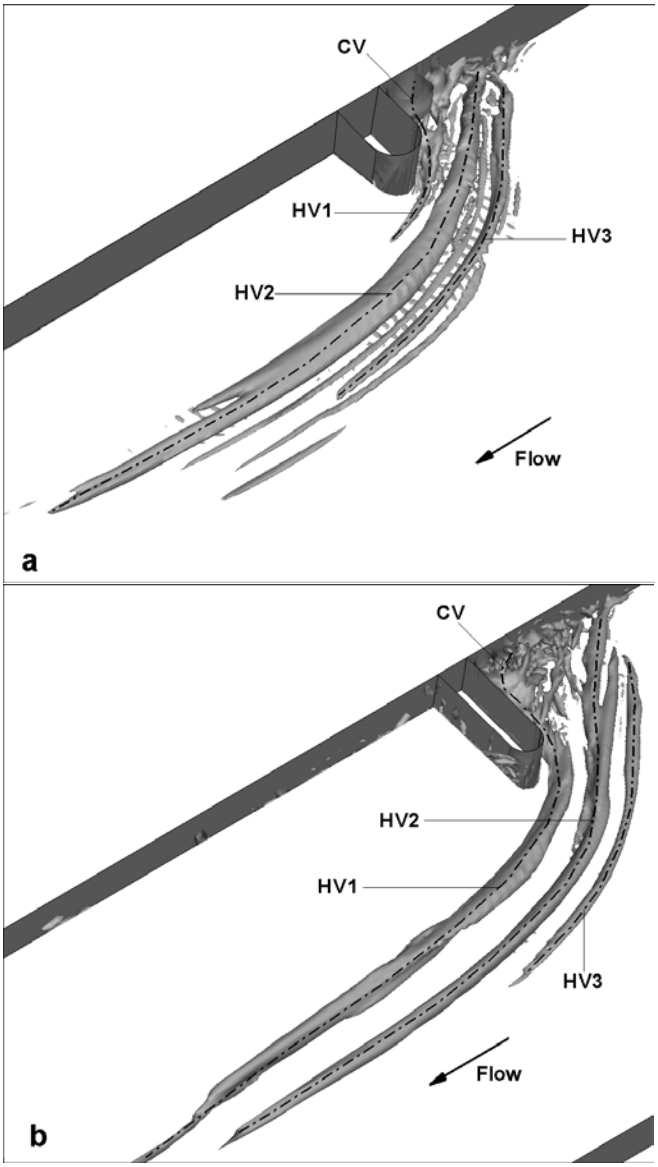

Figure 3. Vortical structures around the abutment for the mean flow visualized by Q criterion for: a) Short-abutment; b) Long-abutment.

Figures 4 and 5 show the streamline patterns superimposed on out-of-plane vorticity contours, and the distribution of the non-dimensional pressure r.m.s. fluctuations $p'^2/(\rho^2 U^4)$ on vertical planes which cut through the HV system for the short and long abutment cases respectively.

In the short abutment case, the turbulent pressure fluctuations are amplified inside the core of HV1 and HV2 for approximately one order of magnitude with respect to the surrounding flow. The level of amplification is similar for these two vortices suggesting that they have similar strengths. However the size of HV1 is considerably smaller than that of HV2. On the other hand, the level of amplification inside the core of HV3 is insignificant at all frames. At sections i-iii, close to the tip of the abutment, a double peaked distribution in the p'^2 is observed inside the core

of HV1 and HV2. This indicates the presence of large scale bi-modal oscillations both for HV1 and HV2. To the best of authors knowledge this is the first time where the bimodal oscillations are observed in the secondary necklace vortex HV2 which wraps around an isolated abutment. At section iv, which is positioned at approximately 1.5D downstream of the abutment, the secondary necklace vortex loses its coherence where the decay in p'^2 inside the core of HV2 is approximately 40%. At this section HV1 is not present as it has already diffused within the flow. The p'^2 has a one peaked distribution inside the core of HV2 at this section indicating that the large scale bimodal oscillations are not present anymore inside the legs of HV2. Note that the large p'^2 values observed on the right hand side at section iv are related to the separated shear layers.

In the long abutment case (see Figure 5) at section i, which is at upstream of the abutment, the amplification in p'^2 inside the core of HV2 and HV3 is negligible compared with the amplification observed inside the core of HV1. At section ii, where the amplification levels both for HV1 and HV2 is largest, the level of amplification inside the core of HV1 is approximately one order of magnitude larger than that of HV2. At this section, compared to the short abutment case, the maximum amplification value inside the core of HV1 is approximately 5 times larger. This suggests that the strength of the main necklace vortex HV1 increases considerably with the increase in the abutment length.

At sections i-iii, inside the core of HV1 $\overline{p'^2}$ is amplified with a double peaked distribution. This is a consequence of the large scale oscillations present at sections close to the tip of the abutment. Similar to the short abutment case the double peaked p'^2 distribution is replaced by a single peaked distribution along the legs of HV1 where the bimodal oscillations are not present any more. This is visualized at section iv which is approximately at 3.4D downstream of the abutment axis.

4.3 *Bed Shear Stress*

The distribution of the non-dimensional mean bed shear stress is given in Figure 6 both for the short and long abutment cases. For the experimental flow conditions the critical non-dimensional bed shear stress is obtained from the Shields diagram as τ_{wc} =0.007. In both cases the largest values of the bed shear stress is obtained close to the tip of the abutment where the flow is accelerating. However large bed shear stress values are also observed beneath the horseshoe vortices (especially beneath the primary necklace vortex, HV1) and the upstream part of the separated shear layers.

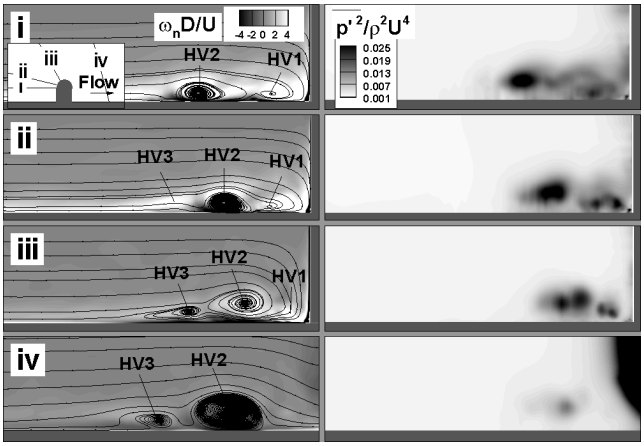

Figure 4. Mean out of plane vorticity contours together with the streamline patterns and resolved pressure r.m.s. fluctuations in representative vertical sections for the short abutment case (see inset in frame i).

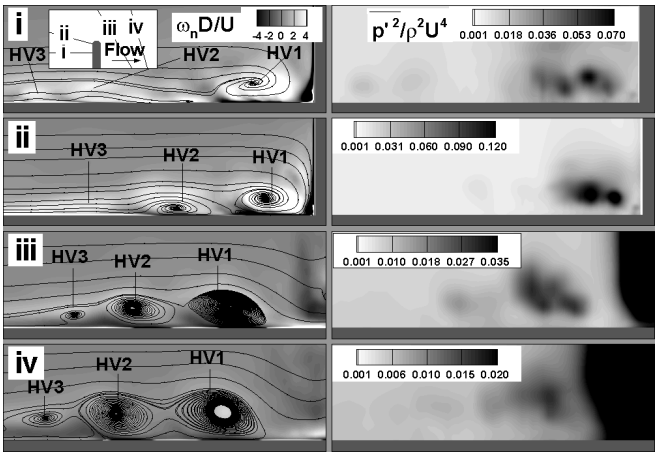

Figure 5. Mean out of plane vorticity contours together with the streamline patterns and resolved pressure r.ms. fluctuations in representative vertical sections for the long abutment case (see inset in frame i).

Although the maximum mean bed shear stress values are comparable in both cases (0.017 in the long abutment case and 0.014 in the short abutment case), which are observed close to the tip of the abutment, there are major differences in the spread of the bed shear stress distribution.

The decay rate of the bed shear stress values within the flow direction is very different for the two cases investigated. In the short abutment case, bed shear stress values which are larger than the threshold value required for sediment entrainment is observed only in the close proximity of the abutment and the bed shear stress values decayed very rapidly in the flow direction. In the long abutment case this decay rate is much slower. Bed shear stress values which are larger than τ_{wc} are observed at a distance up to 7.5D away from the abutment axis in two separate regions beneath the mean location of HV1 and HV2. This is a consequence of the much coherent necklace vortices present in the long abutment case which diffuse much slower within the flow.

In the long abutment case the large bed shear stress values are observed in a region with a wider lateral extent than that of short abutment case. This is related to the size of the primary necklace vortex, HV1, which is larger in the long abutment case.

Another important quantity which determines the sediment entrainment capacity is the non-dimensional r.m.s. pressure fluctuations on the bed which is given in Figure 7 for the short and long abutment cases. In both cases large p'^2 values are recorded around the tip of the abutment beneath the upstream part of the main necklace vortex and especially beneath the separated shear layers. Compared with the short abutment case p'^2 values are approximately two times larger throughout all the amplified regions in the long abutment case. The decay rate of the p'^2 in the flow direction is also faster for the short abutment case.

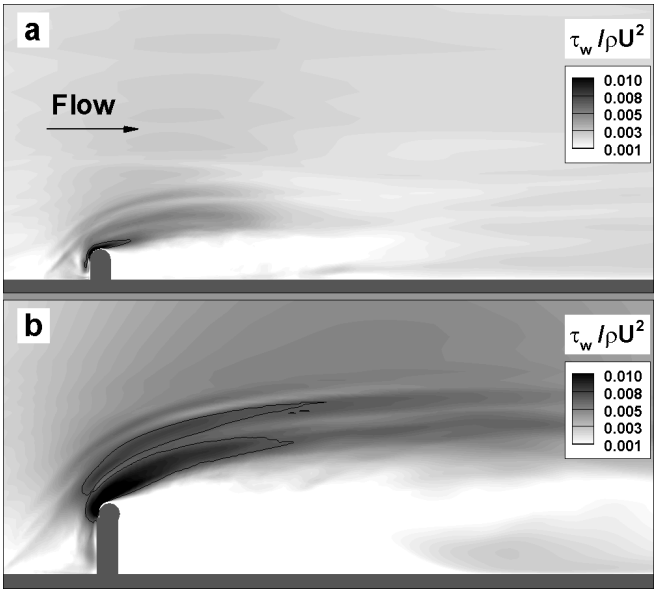

Figure 6. Non-dimensional mean bed shear stress contours for: a) Short-abutment; b) Long-abutment. The solid contour line in frames a corresponds to $\tau_{wc}/\rho U^2=0.007$

5 SUMMARY AND CONCLUSIONS

DES is used in the present study to investigate the changes in the structure of the horseshoe vortex system, differences in the bed shear stress and pressure r.m.s. fluctuations around isolated bridge abutments with different lengths.

For both abutment lengths three necklace vortices are observed which wrap around the abutment. Similar to the findings of Koken and Constantinescu (2008a), in both of these cases the corner vortex CV, which merged with the primary necklace vortex HV1, provided additional fluid and momentum from the regions close to the free surface into the core of the primary necklace vortex HV1.

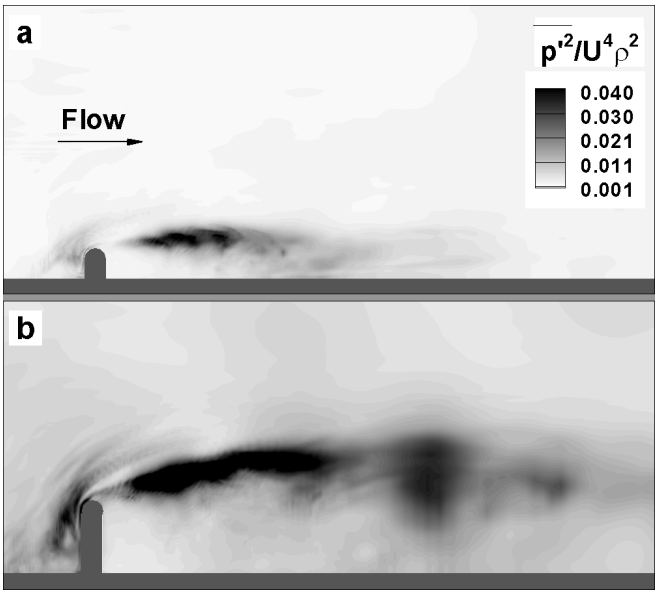

Figure 7. Distribution of the pressure r.m.s. fluctuations at the bed, $p'^2/(\rho^2 U^4)$ for: a) Short-abutment; b) Long-abutment.

Both for the large and short abutment cases the main necklace vortex HV1 was found to undergo bimodal aperiodic oscillations similar to the ones observed in junction flows which was described by Devenport and Simpson (1990). These oscillations significantly amplified the pressure fluctuations within the core of the vortex and were found to peak at sections cutting through the tip of the abutment. Bimodal oscillations disappeared along the legs of HV1 for the long abutment case. A major difference in HV1 for the two cases studied was the length scale over which the main necklace vortex preserved its coherence. For the short abutment case, HV1 completely diffused within the flow at approximately 1D downstream of the abutment axis whereas in the long abutment case HV1 was coherent up to a distance of 17D.

In the long abutment case the strength of the secondary necklace vortex, HV2, was smaller compared to the primary necklace vortex, HV1. However in the short abutment case the secondary necklace vortex was found to have a similar strength with the primary necklace vortex. Moreover, p'^2 contours represented a double peaked distribution for both HV1 and HV2 in the short abutment case suggesting that the aperiodic bimodal oscillations were also present in the core of the secondary necklace vortex HV2.

In both cases the largest values of the bed shear stress is obtained close to the tip of the abutment where the flow is accelerating. However large bed shear stress values are also observed beneath the horseshoe vortices (especially beneath the primary necklace vortex, HV1) and the upstream part of the separated shear layers.

In the short abutment case, bed shear stress values which are larger than the threshold value required for the sediment entrainment is observed only in the close proximity of the abutment and the bed shear stress values decayed very rapidly in the flow direction. In the long abutment case bed shear stress values which are larger than the threshold value is observed in two separate regions elongated in the flow direction. Here the decay rate of the bed shear stress was much slower compared to the short abutment case.

Finally, both for long and short abutment cases, large p'^2 values are recorded around the tip of the abutment beneath the upstream part of the main necklace vortex and especially beneath the separated shear layers. Compared with the short abutment case, p'^2 values are approximately two times larger throughout all the amplified regions in the long abutment case.

ACKNOWLEDGEMENTS

This project is supported by TUBITAK (The Scientific and Technological Research Council of Turkey) under Project No: 108M590 and the computational resources used in this study were partly provided by TUBITAK ULAKBIM High Performance Computing Center, which are gratefully acknowledged here.

REFERENCES

Devenport, W. J., Simpson, R. L. (1990). "Time-dependent and time-averaged turbulence structure near the nose of a wing-body junction." J. Fluid Mech., 210, 23-55.

Melville, B. W. (1997). "Pier and abutment scour: integrated approach." Journal of Hydraulic Engineering, Vol. 123(2), 125-136.

Constantinescu, G. and Squires, K. (2004). "Numerical investigations of flow over a sphere in the subcritical and supercritical regimes." Phys. of Fluids, 16(5), pp. 1449-1466, 2004.

Koken, M. and Constantinescu, G. (2008a). "An investigation of the flow and scour mechanisms around isolated spur dikes in a shallow open channel. Part I. Conditions corresponding to the initiation of the erosion and deposition process." Water Resources Research, 44, W08406, doi:10.1029/2007WR006489.

Koken, M. and Constantinescu, G. (2008b). "An investigation of the flow and scour mechanisms around isolated spur dikes in a shallow open channel. Part II. Conditions corresponding to the final stages of the erosion and deposition process." Water Resources Research, 44, W08407, doi:10.1029/2007WR006491.